Instability growth for magnetized liner inertial fusion seeded by electro-thermal, electro-choric, and material strength effects

J. D. Pecover and J. P. Chittenden

Citation: Physics of Plasmas **22**, 102701 (2015); doi: 10.1063/1.4932328
View online: http://dx.doi.org/10.1063/1.4932328
View Table of Contents: http://scitation.aip.org/content/aip/journal/pop/22/10?ver=pdfcov
Published by the AIP Publishing

Instability growth for magnetized liner inertial fusion seeded by electro-thermal, electro-choric, and material strength effects

J. D. Pecover and J. P. Chittenden
The Centre for Inertial Fusion Studies, The Blackett Laboratory, Imperial College, London SW7 2AZ, United Kingdom

(Received 4 August 2015; accepted 22 September 2015; published online 5 October 2015)

A critical limitation of magnetically imploded systems such as magnetized liner inertial fusion (MagLIF) [Slutz *et al.*, Phys. Plasmas **17**, 056303 (2010)] is the magneto-Rayleigh-Taylor (MRT) instability which primarily disrupts the outer surface of the liner. MagLIF-relevant experiments have showed large amplitude multi-mode MRT instability growth growing from surface roughness [McBride *et al.*, Phys. Rev. Lett. **109**, 135004 (2012)], which is only reproduced by 3D simulations using our MHD code Gorgon when an artificially azimuthally correlated initialisation is added. We have shown that the missing azimuthal correlation could be provided by a combination of the electro-thermal instability (ETI) and an "electro-choric" instability (ECI); describing, respectively, the tendency of current to correlate azimuthally early in time due to temperature dependent Ohmic heating; and an amplification of the ETI driven by density dependent resistivity around vapourisation. We developed and implemented a material strength model in Gorgon to improve simulation of the solid phase of liner implosions which, when applied to simulations exhibiting the ETI and ECI, gave a significant increase in wavelength and amplitude. Full circumference simulations of the MRT instability provided a significant improvement on previous randomly initialised results and approached agreement with experiment. © *2015 AIP Publishing LLC*.
[http://dx.doi.org/10.1063/1.4932328]

I. INTRODUCTION

Magnetized Liner Inertial Fusion (MagLIF)[1,2] represents a promising pathway to controlled thermonuclear fusion; a hollow metallic cylinder or "liner" containing premagnetized and preheated fusion fuel is magnetically imploded on a pulsed power machine. One of the biggest barriers to the success of the scheme is the magneto-Rayleigh-Taylor (MRT) instability,[3,4] which occurs when a fluid is accelerated by a magnetic field and results in implosion asymmetries which reduce confinement and can lead to liner-fuel mix.

Implosions of hollow beryllium liners on the Z generator[5,6] at Sandia National Laboratories carried out by McBride *et al.*[7,8] resulted in higher MRT amplitudes and wavelengths than those predicted by randomly initialised 3D MHD simulations, including the MHD code Gorgon,[9,10] indicating worse than expected performance in terms of confinement and robustness to liner-fuel mix. Code agreement was achieved only with the addition of an artificially azimuthally correlated initialisation. Good agreement between experiment and simulation was, however, achieved for MRT growth from a machined single mode perturbation,[11] suggesting that the poor agreement for randomly initialised liner implosions can be explained by enhanced levels of azimuthal correlation in the experiment over the simulation. This is a key because the MRT modes with the highest growth rate are fully azimuthally correlated.[12]

The development of late time azimuthal correlation can be explained by magnetic tension, which acts to prevent bending of the azimuthal drive magnetic field lines. Consider an array of randomly orientated raised points on the outer surface of a highly conductive medium, such as solid beryllium or a high temperature plasma, as shown in Figure 1(a). The drive magnetic field lines are effectively frozen into the material, so they bend around the perturbations in the radial and axial directions, storing energy through magnetic tension. To minimise this energy, the field lines tend to straighten, and as they are frozen in, they move material. In the radial direction, there is therefore more magnetic pressure applied at the points, decreasing their height, and less magnetic pressure applied to azimuthally adjacent material, allowing it to expand outwards due to its thermal pressure and causing azimuthal correlation. Field line straightening in the axial direction moves the mass of the points axially up or down, causing them to form azimuthally correlated bands (Figure 1(b)), thereby minimising magnetic tension. This axial displacement takes the form of an Alfvén wave and propagates at the Alfvén speed v_a

$$v_a = \sqrt{\frac{B^2}{\mu_0 \rho}}, \tag{1}$$

where B is the local magnetic field, ρ is the density, and μ_0 is the permeability of free space. Physically, the correlation is driven by the magnetic field and damped by the inertia of the plasma mass that must be moved. The inverse density dependence means that low density conductive plasma has a high Alfvén speed and rapidly becomes azimuthally correlated; at solid density, however, the Alfvén speed is low, and the timescale for the development of azimuthal correlation via minimisation of magnetic tension is therefore long. For liner implosions, which in general include a range of plasma densities, it is therefore likely that, if minimisation of

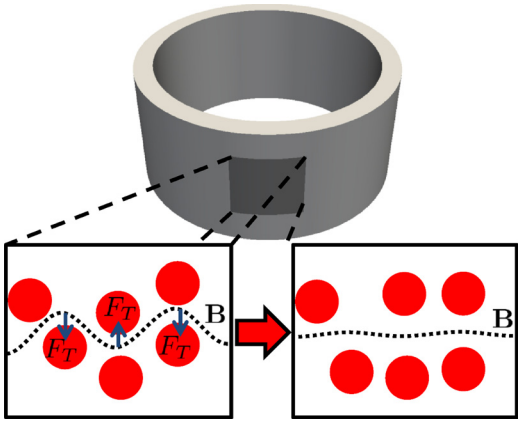

FIG. 1. Development of azimuthal correlation due to magnetic tension in the drive field. As the magnetic field lines bend around the perturbations, a restoring force F_T due to magnetic tension acts at the bends, tending to straighten the field lines.

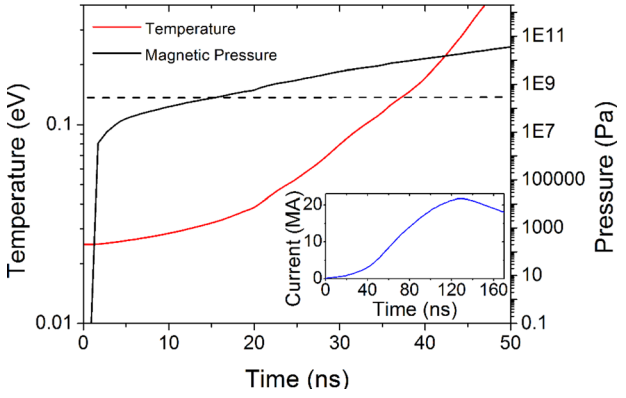

FIG. 2. 1D Gorgon simulation of the experiment of McBride *et al.*, showing the times at which melting temperature and yield stress are exceeded at the liner outer edge. The black dotted line marks both the yield stress and melting temperature; the magnetic pressure (black) exceeds this threshold 21 ns before the temperature (red). Inset is the current pulse used by McBride *et al.*;[7] all timings used in the paper are relative to this.

magnetic tension was the primary source of azimuthal correlation, the lowest density material carrying an appreciable fraction of the current would be the first to become azimuthally correlated. Consider, for example, a beryllium liner with an outer radius of 3.5 mm carrying a current of 10 MA—the timescales for an Alfvén wave to propagate around the liner azimuth, for solid density material (1850 kg/m^3) and low density plasma at 0.01 kg/m^3, would be $\sim 2\,\mu$s and ~ 4 ns, respectively. Once correlation in low density material has developed, MRT growth can subsequently imprint the azimuthally correlated structure onto higher density material.

A possible reason for the under-estimation of late time azimuthal correlation by randomly initialised simulations, as compared to the experiment, is that additional azimuthal correlation can develop early in time in solid regimes through other means. One such mechanism is the electro-thermal instability (ETI).[13,14] This instability is driven by temperature dependent resistivity and alters the distribution of both current density and temperature within the liner. In the solid state, the current forms azimuthally correlated bands, which have the same orientation of wavevector as the fastest growing MRT modes. Thermal conduction and resistive diffusion, however, limit the ETI amplitude and it is the "electrochoric instability" (ECI), which amplifies microscopic variations in density as the liner outer edge vapourises, that provides a high amplitude, azimuthally correlated seed for the MRT instability.

An additional effect not included in previous Gorgon simulations is material strength. Although there is no strength remaining during the MRT growth phase, the liner is still solid during the early time ETI and ECI development stages where material strength may be important. A Gorgon simulation was carried out to estimate its significance—a 1D MHD simulation was initialised using the liner and current drive parameters from McBride *et al.* (hollow beryllium liner with an outer radius of 3.47 mm and thickness of 580 μm, imploded by an approximately 150 ns, 22 MA peak current), and the surface temperature and magnetic pressure of the liner monitored. Figure 2 shows that the liner outer edge initially yields not because of melt, but because the yield stress of beryllium is exceeded; strength can therefore have an effect and should be included for a physical treatment of the solid phase of the liner.

In this paper, we use the MHD code Gorgon, running in 3D cylindrical (r-θ-z) geometry to investigate the physical processes and instability development during MagLIF-relevant liner implosions. In Sec. II, we explain how the ETI causes early time azimuthal correlation, arising both from single point and random perturbations. We explain how the ECI develops around vapourisation in Sec. III, where we also present simulation results showing how the ECI is seeded by the ETI and how the ECI subsequently seeds the MRT instability. In Sec. IV, we present details of the material strength model added to Gorgon, and in Sec. V we apply it to full circumference liner implosions, demonstrating how its inclusion is important even for effects which are observed after the entire liner has melted. We show a comparison with the experimental results from Ref. 7, demonstrating improved agreement when the ETI, ECI, and material strength are included.

II. THE ELECTRO-THERMAL INSTABILITY

An ETI occurs when a material with temperature dependent resistivity is Ohmically heated. A mathematical model of the ETI developed by Ryutov *et al.*[12] and subsequently Peterson *et al.*[13] reveals that the morphology of resultant structures is dependent on the sign of the derivative of resistivity with respect to temperature ($\frac{\partial \eta}{\partial T}$). If $\frac{\partial \eta}{\partial T} < 0$ and resistivity decreases with temperature, as in a plasma with Spitzer-like resistivity, current channels or "filaments" tend to form in the axial direction. On the other hand, if $\frac{\partial \eta}{\partial T} > 0$ and resistivity increases with temperature, such as for metals in the solid state, azimuthally correlated bands or "striations" form; this subset of the ETI is also referred to as the "overheat instability"[15,16] and is the form of the ETI considered in this paper. Figure 3 shows regions in density-temperature space for beryllium at solid density susceptible to striations (a) and beryllium at low density susceptible to filaments (b).

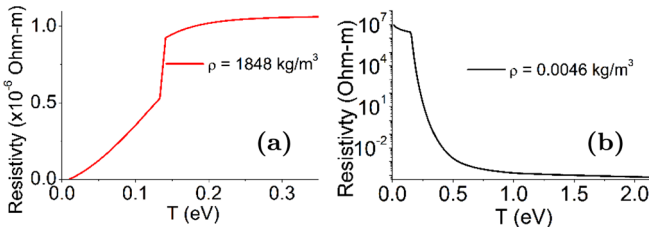

FIG. 3. Resistivity as a function of temperature for beryllium at solid density (a) and low density (b), susceptible, respectively, to striations and filaments.

The dispersion relation for striations with an axial current density, $\mathbf{J} = (0,\ 0,\ J_z)$, according to the mathematical model[13] is

$$\Gamma = \frac{1}{\rho c_v}\left[\frac{\partial \eta}{\partial T} J_z^2 - k^2 \kappa\right], \tag{2}$$

where Γ is the growth rate, ρ is the mass density, c_v is the heat capacity, k is the ETI wavenumber, and κ is the thermal conductivity. The signs of the terms in the dispersion relation reflect the fact that the instability is driven by current and temperature-dependent resistivity and stabilised by thermal conduction. Setting the growth rate to zero yields the critical wavenumber for striations, converting to wavelength gives

$$\lambda_c = 2\pi \sqrt{\frac{\kappa}{\frac{\partial \eta}{\partial T} J_z^2}}. \tag{3}$$

Perturbations below this wavelength are stabilised by thermal conduction, so this sets the minimum wavelength of the ETI. As the model assumes that all current flows on the surface of the conductor, it neglects the phenomenon of resistive diffusion which provides an additional dissipative term; in reality this provides an additional stabilisation term for the outermost portions of the liner that is not reproduced by this mathematical model.

A. Single point test problem

A 3D test problem to explain the tendency of the ETI to cause azimuthal correlation was run using Gorgon. A wedge of solid, cold beryllium in cylindrical geometry was perturbed by raising the temperature of a single hemispherical volume at the outer edge. The hemispherical volume was chosen to be much larger than both the grid resolution of the simulation and the critical ETI wavelength predicted by Eq. (3), to ensure both a single mode instability and resolution of the ETI. Material movement was switched off, to highlight the effect of resistive diffusion and ensure that the effects observed were electro-thermal in origin, with no dependence on density. Figure 4 shows the initialisation for the test problem with the subsequent evolution of current density and temperature.

As the perturbed region has a higher temperature, it also has a higher resistivity than the unperturbed volume. When the axial current is applied, less current therefore flows through the hemisphere and, as shown in Figure 4(b), is instead redirected to more conductive paths either side of the perturbation in the azimuthal direction. Resistive diffusion is also higher through the hemisphere, so the current density is higher in the region radially interior to the hemisphere, relative to unperturbed regions at the same radial position.

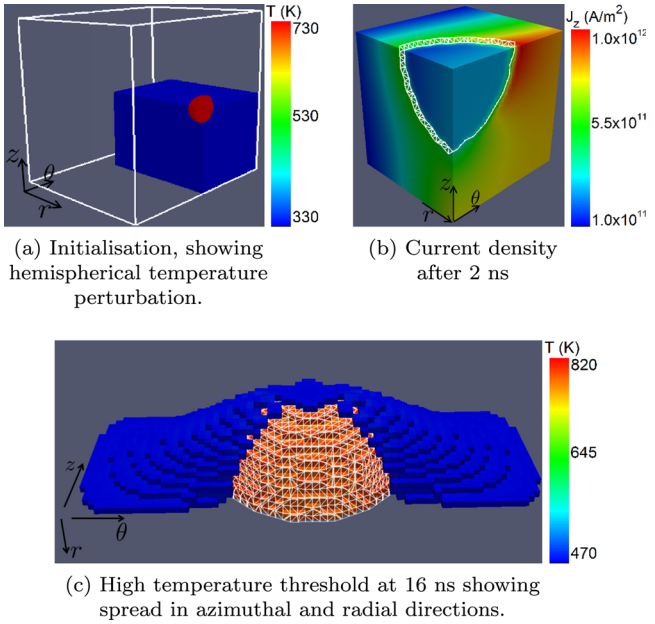

(a) Initialisation, showing hemispherical temperature perturbation.

(b) Current density after 2 ns

(c) High temperature threshold at 16 ns showing spread in azimuthal and radial directions.

FIG. 4. 3D Gorgon test problem demonstrating how current flow around a temperature perturbation leads to azimuthal correlation. The white mesh on (b) and (c) shows the position of the initial perturbation.

The areas of enhanced current density initially have the same resistivity as the unperturbed region; however as the rate of Ohmic heating is proportional to ηJ^2, these areas heat at a faster rate and become more resistive. This causes the regions of higher current to extend further in the azimuthal and radial directions, continuing to Ohmically heat so that the hot hemisphere elongates in the azimuthal and radial directions as shown in Figure 4(c). An array of randomly orientated hot hemispheres, each growing in the azimuthal and radial directions via this effect, would soon develop into azimuthally and radially correlated bands of alternating high and low temperature growing from the liner outer edge.

B. Random initialisation

The development of a multi-mode ETI was investigated by initialising a 3D Gorgon simulation at an axial resolution of 2 μm with material movement switched off with a random temperature perturbation on the cell size at the outer edge. The results show that the magnitude of the temperature perturbation, defined as the difference in temperature between the hot and cold bands, never exceeds the amplitude of the initial perturbation; this can be explained physically by resistive diffusion. As resistivity increases with temperature during the development of the ETI, the axial locations of hot, azimuthally correlated bands are more resistive than adjacent cold bands. Resistive diffusion is therefore greater at the locations of the hot bands, resulting in a lower current density at the liner surface, and a higher current density deeper down. In the outermost few microns of the liner, bands of high temperature correspond to bands of low current density, Ohmically heating at a slower rate than adjacent cold bands

and therefore reducing the temperature difference between them; these radial regions are locally stable to the ETI.

Deeper down, however, the higher rate of resistive diffusion in the hot bands means that bands of high temperature correspond to bands of high current density. The hot bands here are therefore Ohmically heated more than adjacent cold bands, increasing the ETI amplitude—these radial regions are locally unstable to the ETI. When investigating the development of azimuthal correlation, a depth of 30 μm was chosen, such that the area investigated was well within the unstable region.

Figure 5 shows the development of azimuthal correlation 30 μm in from the liner outer edge due to electro-thermal effects early in the current pulse. By 30 ns, the high resolution random initialisation has been smeared out due to the diffusive effect of thermal conduction, resulting in a collection of hot and cold spots corresponding to areas of higher and lower current density, respectively. As a result of the same mechanism by which the single hemisphere spread out azimuthally in Sec. II A, the approximately circular hot spots elongate in the azimuthal direction over the next 30 ns, developing a high level of azimuthal correlation by 62 ns. For all the times shown, the current density and temperature maps are well correlated with each other, as expected based on the electro-thermal origin of the developing azimuthal correlation. As material movement is switched off, this development of correlation cannot be caused by the MRT instability or other density dependent effects.

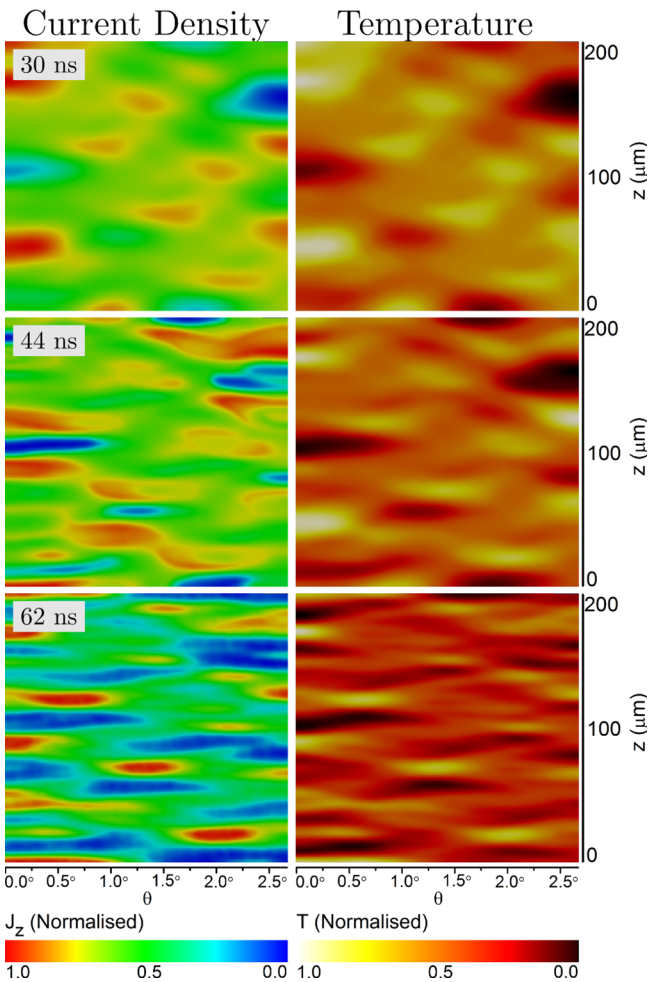

FIG. 5. Normalised current density and temperature maps showing the development of azimuthal correlation from a random perturbation due to the ETI.

III. THE ELECTRO-CHORIC INSTABILITY

The ECI is the name we have chosen to describe the strong amplification of the ETI amplitude around vapourisation; the strong dependence of resistivity on density causes the formation of macroscopic, azimuthally correlated "fingers" of alternating high and low density at the ETI wavelength. The mechanism of the ECI can be explained with reference to the bulk material dynamics of metals.

A. Physical explanation

Figure 6(a) shows the solid density pressure isochore of beryllium as a function of temperature, calculated using the Frankfurt Equation Of State (FEOS)[17–19] data used by Gorgon. Below the vapourisation temperature, the pressure is effectively zero so there is minimal expansion of the liner. As the liner outer edge is Ohmically heated to the vapourisation temperature, the pressure increases by over 6 orders of magnitude to 10 GPa, causing a rapid expansion of the liner outer edge and hence a rapid drop in the density of the vapourised material as it expands. The sharpness of the transition is not entirely physical, as in reality the liner is heated approximately isentropically rather than isochorically, and thermal expansion causes the density to drop prior to vapourisation; it is also sensitive to the equation of state model used.

Figure 6(b) shows the vapourisation temperature resistivity isotherm as a function of density taken from the Lee-More-Desjarlais transport coefficient data[20,21] used by Gorgon. Resistivity gradually increases as density decreases from solid density down to about 600 kg/m^3, below this density the resistivity increases by over an order of magnitude for each halving of the density. This strong "electro-choric" dependence causes the current flowing at the liner outer edge to resistively diffuse at a faster rate, rapidly cascading the current to deeper, unvapourised regions of the liner. The combination of these strong dependencies results in a sudden increase in amplitude of microscopic temperature and current variations at the liner outer edge, such as those formed by the ETI.

Consider the liner just before the outer edge vapourises (Figure 7(a)): in the axial direction, there are alternating hot and cold azimuthally correlated bands formed by a low

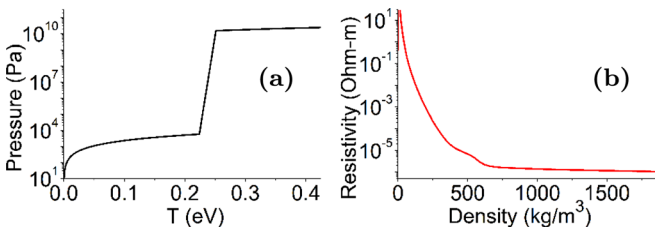

FIG. 6. Pressure as a function of temperature for beryllium at solid density (left) and resistivity as a function of density for beryllium at the solid density vapourisation temperature (right).

amplitude ETI. The hotter bands vapourise slightly earlier than the cold bands, so there will be a short period of time δt where only the hotter bands have vapourised (Figure 7(b)). Consider the physical processes which occur within δt—as the hot bands vapourise the pressure increases by several orders of magnitude, triggering a rapid expansion and corresponding decrease in density. This density decrease results in a massive increase in resistivity, causing the current to rapidly diffuse into the liner just ahead of the vapourisation front. The former positions of the hot bands therefore become low density voids between the cold bands, which form higher density "spikes." The process of vapourisation of the hot bands does not continue indefinitely; for deeper liner positions, the low density but high pressure material further out tamps the expansion, reducing the electro-choric effect.

In order for the cold bands to vapourise, the current would have to follow the shapes of the cold, high density spikes as shown in Figure 7(b), flowing along very bent paths. However, as the total resistance of a current path radially interior to the spikes is lower, primarily because the total path length is shorter as a result of bypassing the spikes, this path is preferentially chosen and the bulk current diffuses radially into the liner, becoming highly uniform in the axial direction. This causes the Ohmic heating rate of the tips of the spikes to fall dramatically; the spikes therefore persist for several tens of nanoseconds and provide a high amplitude, azimuthally correlated seed for the MRT instability.

The vapourised material ejected exterior to the hot bands is initially unionised and resistive, and as it is produced at high pressure and low density, quickly expands axially and azimuthally as well as radially, smearing out any structure with which it was initially imprinted.

B. 3D Gorgon simulation to observe coupling of the ETI, ECI, and MRT instability

A Gorgon simulation with a resolution of 2 μm at the liner outer edge was run in 3D wedge geometry with material movement switched on, to observe development of the ECI (Figure 8) and the subsequent seeding of the MRT instability from the resulting structures (Figure 9).

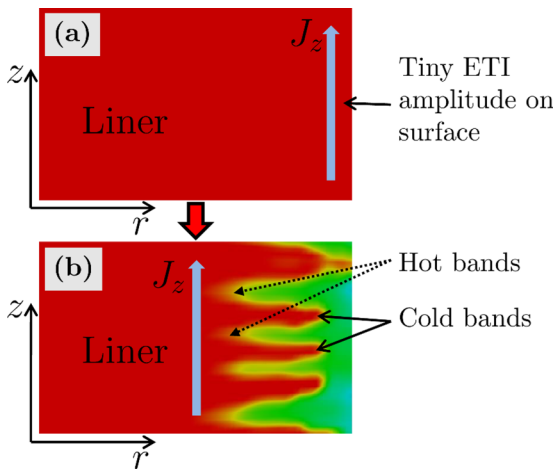

FIG. 7. Explanation of the development of the ECI from the ETI at vapourisation.

Once the liner outer edge begins to vapourise, the growth of the ECI can be observed. Figure 8 shows density slices in the *r-z* plane and contour plots of three different densities, coloured by their current density at three times during the development of the ECI. The densities chosen for the contours are 100 kg/m^3, the density in which the maximum ECI amplitude occurs; 3 kg/m^3, a low density contour that is highly resistive when the ECI is seeded; and 630 kg/m^3, the contour in which the ECI is first visible.

The ECI becomes visible in the *r-z* density slices and 630 kg/m^3 contour at 60 ns and can be identified by the small ripples which appear at the interface between the high density liner outer edge and low density vapour and the azimuthally correlated bands in the contour. As the 3 kg/m^3 contour is largely unionised, it is highly resistive and carries very little current, so has little effect on the bulk dynamics at this point. As shown in Figure 6(b), the resistivity of expanding beryllium at the vapourisation temperature increases sharply when the density drops below ~600 kg/m^3, so it is conductive material above this density that carries the majority of the current. The early development of the ECI occurs here, where a small decrease in density results in a large increase in resistivity. As the bulk temperature increases, the density that this rapid change occurs at decreases, and the largest ECI amplitude occurs at a density of 100 kg/m^3.

The liner outer edge expands rapidly over the next 10 ns, reaching its maximum radius at 70 ns—by this point the ECI spikes are well developed, with an average peak to valley amplitude of the order 50 μm. Further expansion of the high density contours is tamped by exterior hot material, so although they carry a high current there is little change in their structure—the contour at 630 kg/m^3 retains the azimuthally correlated structure, which forms around vapourisation, until ~110 ns, which is well into the MRT growth phase.

Although the contour at 3 kg/m^3 is cold and highly resistive at 60 ns, it has a small heat capacity so is quickly heated and ionised, becoming a hot and highly conductive plasma by 70 ns. As it is accelerated radially inwards by the azimuthal drive field, it is pushed against more dense liner material, which is highly azimuthally correlated due to the ECI and immediately imprints its structure onto the low density material. This is the point at which the ECI seeds the MRT instability; after this, the low density material is highly azimuthally correlated and unstable to the MRT instability, which increasingly dominates the bulk dynamics.

The axial wavelength in the 3 kg/m^3 contour, now determined by the MRT instability, roughly doubles over the next 8 ns, growing independently of the remnant ETI wavelength which is still visible in the 630 kg/m^3 contour. The high current density in the outer, low density plasma causes it to compress onto progressively higher density material, imprinting the MRT instability structure and azimuthal correlation. As the compressive forces are applied at the tips of the spikes, any small inhomogeneities in the *z* direction grow, causing the spikes to bend and merge with neighbouring spikes and increasing the overall axial wavelength.

Figure 9 shows the further development of the 3 kg/m^3 and 630 kg/m^3 contours from Figure 8. The MRT instability

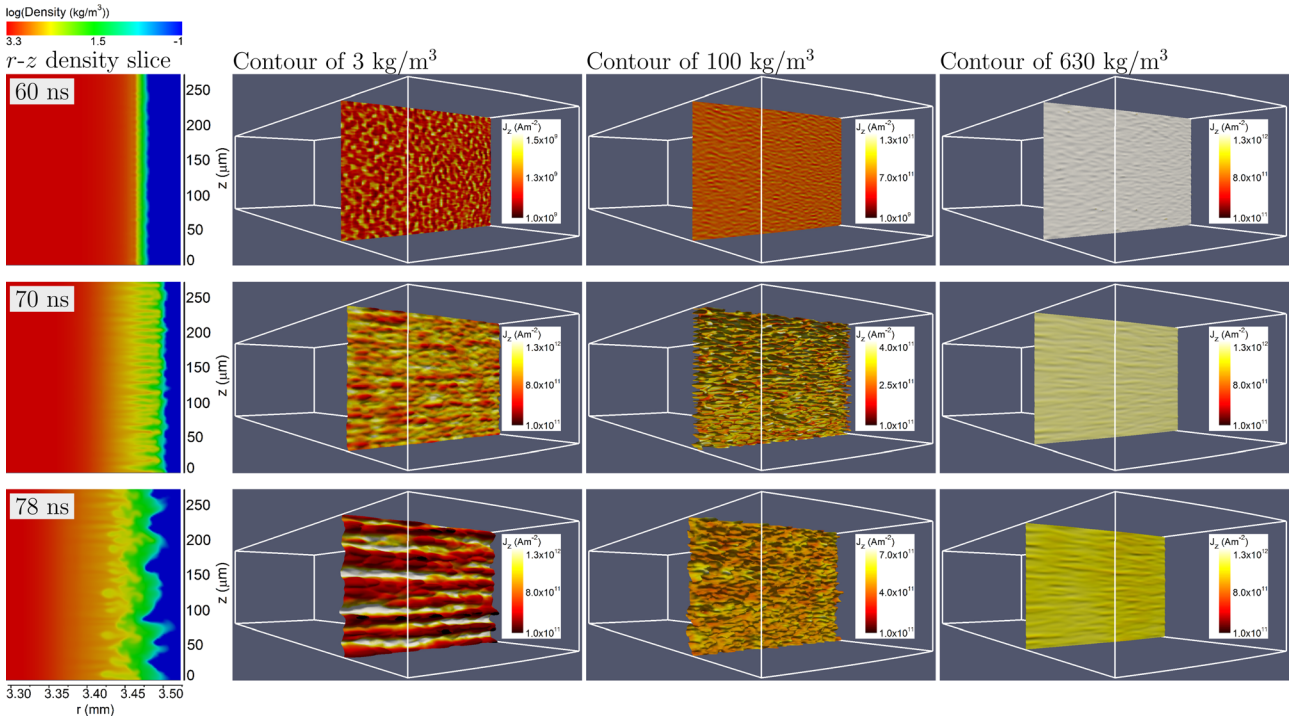

FIG. 8. Results from a 3D Gorgon simulation showing the behaviour of mass and current density during the development of the ECI from just before vapourisation to a few ns after.

grows rapidly in the 3 kg/m^3 contour, with the wavelength having increased to around half the axial domain size by 96 ns—this places a limit on the maximum MRT wavelength; a further cascade to longer wavelengths would require an axial domain a few times longer than the dominant MRT wavelength at the time of interest. The long wavelength structure from the 3 kg/m^3 contour is imprinted onto the 630 kg/m^3 contour as it is recompressed; by 108 ns, the structure is visible in the current density, and by 128 ns the MRT instability structure has imprinted onto the mass density. Some of the

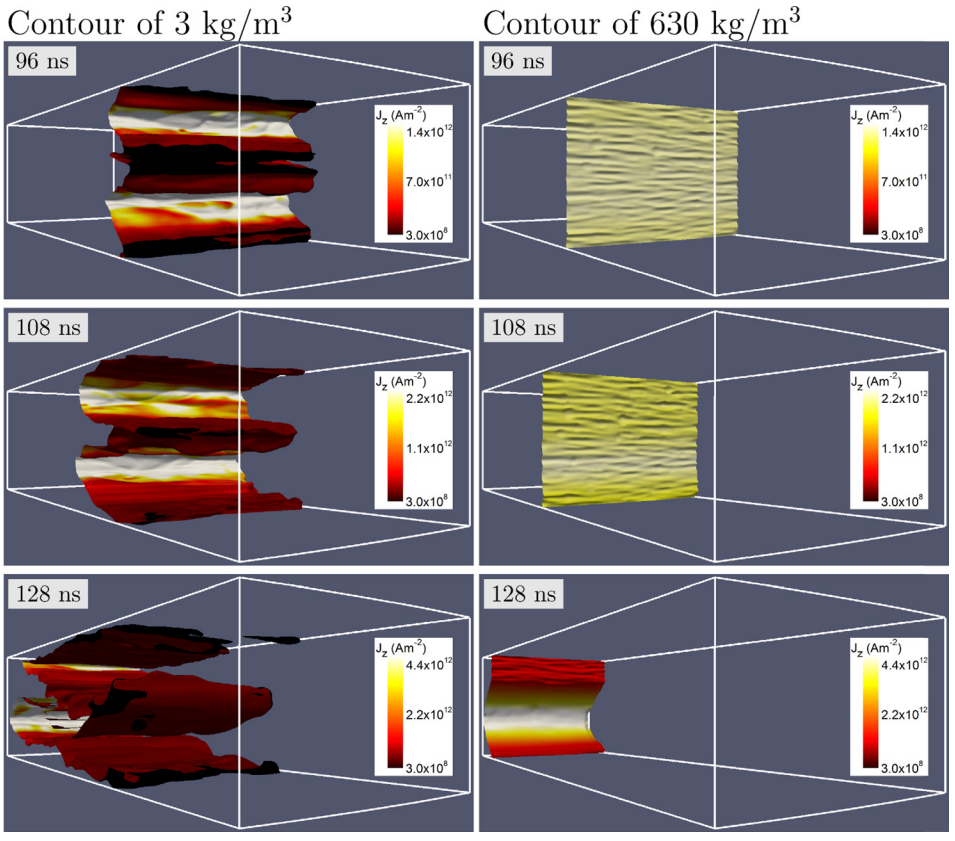

FIG. 9. High and low density contours showing the development of the MRT instability from the ECI.

ECI structures are still visible in the 630 kg/m^3 contour; these structures, however, do not grow during the MRT phase and are eventually obliterated by the long wavelength, high amplitude MRT structure resulting from recompression of low density plasma.

IV. MATERIAL STRENGTH MODEL

In order to better model the solid phase of the liner and resolve the melt transition early in time, a material strength model was added to Gorgon. The additional forces and work done resulting from strength were incorporated into the hydrodynamics equations, following the method employed to model viscous forces in the hydrodynamics code SALE,[22] and later material strength in the shock physics codes SALES_2[23] and iSALE.[22,24,25] An elastic-plastic model was used for material deformation, with yield stress calculated using the Johnson-Cook model[26] and plastic deformation modelled by capping the stress components using the second invariant of the stress tensor.[27–29] Gorgon with the material strength model was subsequently benchmarked against iSALE.

A. Coupling to the MHD equations

The couplings to the MHD equations for the shear forces supported by viscosity are identical in form to those supported by material strength in the solid phase; therefore in order to add material strength, an MHD model is constructed with an anisotropic pressure term capable of supporting viscosity. The MHD equations for momentum and energy are then given by

$$\rho\frac{\partial \mathbf{v}}{\partial t}+\mathbf{v}.\nabla\mathbf{v}=-\nabla P+\mathbf{J}\times\mathbf{B}+\nabla.\underline{\underline{s}}, \tag{4}$$

$$\frac{\partial U}{\partial t}+\mathbf{v}.\nabla U=-P\nabla.\mathbf{v}-\nabla.\mathbf{q}+\eta|\mathbf{J}|^2+\underline{\underline{s}}:\nabla\mathbf{v}, \tag{5}$$

where $\underline{\underline{s}}$ is the stress tensor without the contribution from pressure, which is included separately as a scalar quantity. All nine components of the stress tensor must be calculated for a 3D model.

Figure 10 shows the components of the stress tensor $\underline{\underline{s}}$, expressed in 3D Cartesian geometry. The stress tensor can be represented by the index notation s_{ij}, where the first index refers to the face of the cell being considered, and the second index refers to the direction of the stress. The $\nabla.\underline{\underline{s}}$ force in the momentum equation (Equation (4)) and $\underline{\underline{s}}:\nabla\mathbf{v}$ work term in the energy equation (Equation (5)) are analogous to the pressure gradient force and $P\nabla.\,\mathbf{v}$ work term, respectively. In Cartesian geometry, these can be expanded to give the force vector (Equation (6)) and additional work term (Equation (7))

$$\begin{aligned}F_x&=\frac{\partial s_{xx}}{\partial x}+\frac{\partial s_{xy}}{\partial y}+\frac{\partial s_{xz}}{\partial z},\\ F_y&=\frac{\partial s_{xy}}{\partial x}+\frac{\partial s_{yy}}{\partial y}+\frac{\partial s_{yz}}{\partial z},\\ F_z&=\frac{\partial s_{xz}}{\partial x}+\frac{\partial s_{yz}}{\partial y}+\frac{\partial s_{zz}}{\partial z},\end{aligned} \tag{6}$$

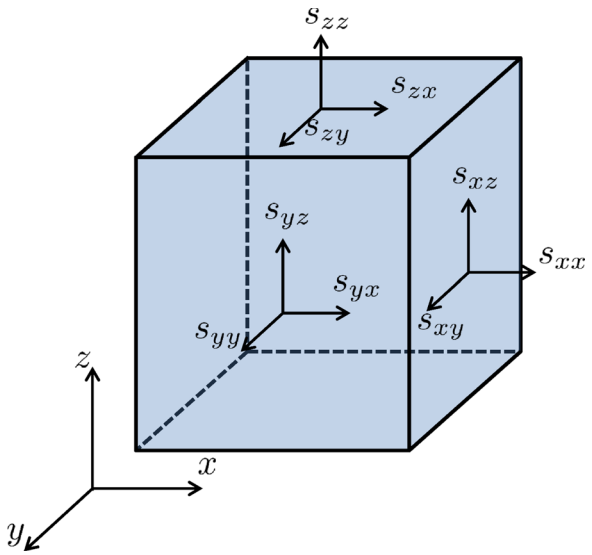

FIG. 10. Diagram showing orientation of the nine independent components of the stress tensor in Cartesian geometry.

$$\begin{aligned}\underline{\underline{s}}:\nabla\mathbf{v}=&\,s_{xx}\frac{\partial v_x}{\partial x}+s_{xy}\frac{\partial v_x}{\partial y}+s_{xz}\frac{\partial v_x}{\partial z}\\ &+s_{xy}\frac{\partial v_y}{\partial x}+s_{yy}\frac{\partial v_y}{\partial y}+s_{yz}\frac{\partial v_y}{\partial z}\\ &+s_{xz}\frac{\partial v_z}{\partial x}+s_{yz}\frac{\partial v_z}{\partial y}+s_{zz}\frac{\partial v_z}{\partial z}.\end{aligned} \tag{7}$$

B. Calculation of the stress tensor

In order to calculate the stress tensor, the strainrate tensor $\dot{\underline{\underline{\epsilon}}}$ which describes the degree of velocity shear in 3D must first be calculated; this is defined by

$$\dot{\epsilon}_{ij}=\frac{1}{2}\left(\frac{\partial v_i}{\partial x_j}+\frac{\partial v_j}{\partial x_i}\right), \tag{8}$$

which is by definition symmetric, meaning that there are only six independent components; this also applies to the stress tensor. The strain rate tensor can be expanded in Cartesian geometry to give

$$\dot{\underline{\underline{\epsilon}}}=\begin{pmatrix}\frac{\partial v_x}{\partial x} & \frac{1}{2}\left(\frac{\partial v_x}{\partial y}+\frac{\partial v_y}{\partial x}\right) & \frac{1}{2}\left(\frac{\partial v_x}{\partial z}+\frac{\partial v_z}{\partial x}\right)\\ \frac{1}{2}\left(\frac{\partial v_x}{\partial y}+\frac{\partial v_y}{\partial x}\right) & \frac{\partial v_y}{\partial y} & \frac{1}{2}\left(\frac{\partial v_y}{\partial z}+\frac{\partial v_z}{\partial y}\right)\\ \frac{1}{2}\left(\frac{\partial v_x}{\partial z}+\frac{\partial v_z}{\partial x}\right) & \frac{1}{2}\left(\frac{\partial v_y}{\partial z}+\frac{\partial v_z}{\partial y}\right) & \frac{\partial v_z}{\partial z}\end{pmatrix}. \tag{9}$$

A key difference between solids and viscous fluids is that in solids, stress is accumulated over time; the stress tensor must therefore be treated as an integrated quantity with knowledge of its history, so the relationship between stress and strain rate is a differential equation. The change in stress is related to the strain rate through the shear modulus G

$$\frac{\partial s_{ij}}{\partial t}=2G\left(\dot{\epsilon}_{ij}-\delta_{ij}\dot{\epsilon}_{ii}\right), \tag{10}$$

where δ_{ij} is the Kronecker delta function. The accumulated stress is calculated by integrating this equation with respect to time. The shear modulus for elastic deformation is in general a function of density and temperature and is related to the bulk modulus $K(\rho, T)$ via the material specific Poisson Ratio ν

$$G(\rho,T) = 3K(\rho,T)\frac{1-2\nu}{2(1+\nu)}. \tag{11}$$

The bulk modulus as a function of density and temperature is calculated along the isentropes of the equation of state $P(\rho, T)$

$$K(\rho,T) = \rho\frac{\partial P(\rho,T)}{\partial \rho} = \rho\, c_s^2(\rho,T). \tag{12}$$

C. Modelling plastic deformation

For most metals, deformation is elastic for small stresses but at larger stresses the deformation becomes plastic and the shear modulus becomes stress-dependent, Equation (10) therefore becomes non-linear and difficult to solve. Continuing to use this relation once the yield stress has been exceeded causes the stress in each timestep to exceed the maximum physically permitted stress, as the stress in the plastic phase is always lower than if the elastic phase was extrapolated forward indefinitely. A well established mathematical method to correct for this is to subsequently limit the stress to the dynamic yield stress.[27–29] To do so, an appropriate scalar magnitude must be constructed to allow a comparison with the scalar yield stress; we use J_2, the second invariant of the stress tensor, defined in Cartesian geometry by[27]

$$J_2 = \frac{1}{2}\left(s_{xx}^2 + s_{yy}^2 + s_{zz}^2\right) + s_{xy}^2 + s_{xz}^2 + s_{yz}^2, \tag{13}$$

which takes into account all of the stress components. The second invariant of the stress tensor is then compared to the square root of the yield stress Y, and if it is greater, then all stress components are multiplied by a factor $Y/\sqrt{J_2}$, remapping the stress tensor onto the yield envelope. The plastic strain rate is calculated by taking the difference between the stress before and after the remap and converting it to an equivalent strain rate via Equation (10). This is stored and accumulated as integrated plastic strain, important for calculation of the yield stress.

Two obvious ways in which the yield stress varies are thermal softening and work hardening. Thermal softening is the result of strongly bound metal ions gaining thermal energy, weakening their bonds, and reducing the activation energy required to break them; this effect also causes the bulk modulus to decrease. Work hardening is the process where the energy from strain also goes into moving dislocations within a material, causing them to align and therefore making the material able to withstand a higher level of strain.

D. Yield calculation: Johnson-Cook model

The Johnson-Cook model[26] is an empirical model that calculates yield stress Y as a function of temperature, accumulated plastic strain, and instantaneous plastic strain rate, taking into account thermal softening and work hardening. Equation (14) shows the empirical formula for calculating yield stress

$$Y = (A + B\epsilon_p^n)(1 + C\ln(\dot{\epsilon}_p^*))(1 - (T/T_{melt})^n), \tag{14}$$

where $\dot{\epsilon}_p^*$ is the dimensionless plastic strain rate defined as $\dot{\epsilon}_p^* = \dot{\epsilon}_p/\dot{\epsilon}_{p0}$ with $\dot{\epsilon}_{p0} = 1\,\mathrm{s}^{-1}$; T_{melt} is the melting temperature in Kelvin; and A, B, C, m, and n are material specific constants.

V. MATERIAL STRENGTH APPLIED TO MagLIF

In order to analyse the effect of material strength on MagLIF-relevant liner implosions, wedge simulations were carried out both with and without strength at 2 μm resolution, sufficient to resolve the ETI. This high resolution allowed only a small fraction of the liner volume to be simulated under the requirement of a reasonable computational run time.

A. The effect of material strength on the ETI

As the liner heats up and melts, it loses strength from the outer edge inwards due to the effect of thermal softening and melt; Figure 11 shows the radial extent of the liner that has melted as a function of time, measured radially inwards from the outer edge.

The liner outer edge loses strength at 36 ns; the depth that has lost strength subsequently increases at an almost constant rate of ~10 μm/ns. For previous simulations without strength (Sec. III B), the ECI becomes visible at 60 ns and reaches its maximum expansion at 70 ns; at these times, the depths that have lost strength are, respectively, ~200 μm and ~300 μm. It is therefore difficult to see how material strength can directly affect the ECI as the liner outer edge vapourises (this begins around 60 ns, see Figure 8). However, prior to its melting (when strength is lost), the liner outer edge is susceptible to the ETI and retains strength, which can affect ETI development until 36 ns, and deeper into the liner at later times. It is interesting to observe the outermost point in the liner that still has strength, as this should correspond to the

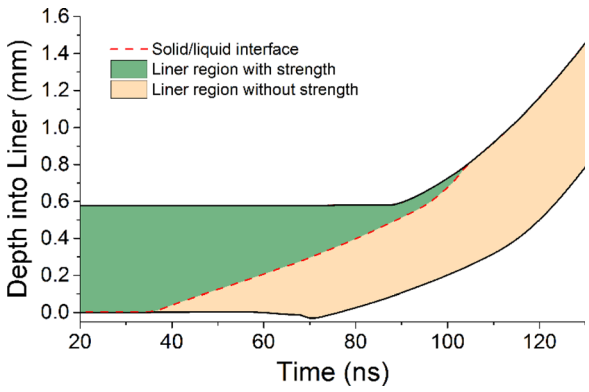

FIG. 11. 1D simulation result showing which regions of the liner have strength, plotted as a function of time. Depth into the liner is defined relative to the initial position of the liner outer edge at 0, with the initial position of the liner inner edge at 0.58 mm.

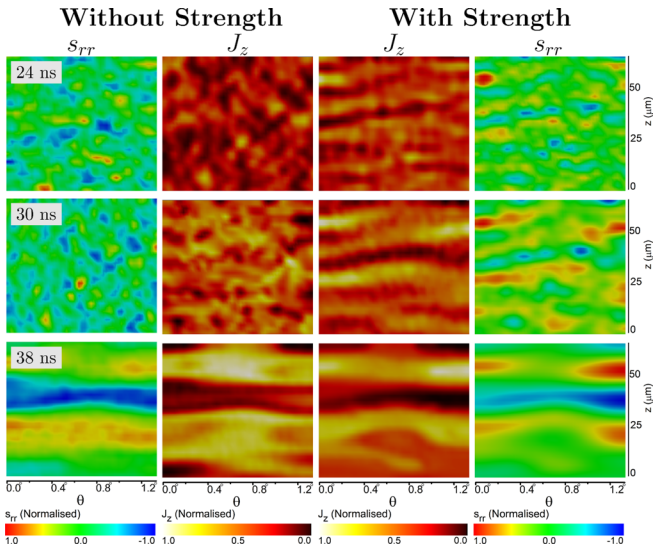

FIG. 12. Development of azimuthal correlation in individually normalised maps of J_z and s_{rr} at the outermost part of the liner that still has strength, and comparison to equivalent radial position in simulation without strength. Stress is used only as a diagnostic in the latter.

maximum ETI amplitude where strength directly plays a role.

A comparison was carried out between simulations with and without strength; Figure 12 shows 2D maps of current density and s_{rr} in the θ–z plane at the outermost point in the liner that still has strength. The latter is the cylindrical geometry equivalent of s_{xx} in planar geometry, and it shows structures similar to those observed in 2D maps of J_2 (Eq. (13)), which is a function of all six stress components. s_{rr}, however, is signed, allowing an indication of whether each point is locally under compression or rarefaction in the radial direction.

Figure 12 shows that material strength enhances the level of azimuthal correlation during the development of the ETI; this occurs because of positive feedback between the ETI and the strength model—strength results in the banded structure propagating faster into the liner, further locking in developing azimuthal correlation and differences between axially adjacent bands. An additional result of this feedback is a higher ETI amplitude; by 38 ns, the difference in current density between adjacent bands is a factor of three greater for the simulation with strength. The tendency of shear forces to resist bending, smoothing out short wavelength perturbations and setting a longer wavelength, also enhances azimuthal correlation via a similar mechanism to the magnetic tension in Figure 1; this should additionally result in a longer axial wavelength when strength is included, as observed. This wavelength difference is apparent as the ECI develops (Figure 13).

B. The effect of material strength on the ECI

The effect of material strength is still apparent when the liner outer edge begins to vapourise; Figure 13(a) shows density slices taken from simulations with and without material strength, at radial and axial resolutions of 2 μm and azimuthal resolution of 0.1°. Quantitative comparisons between

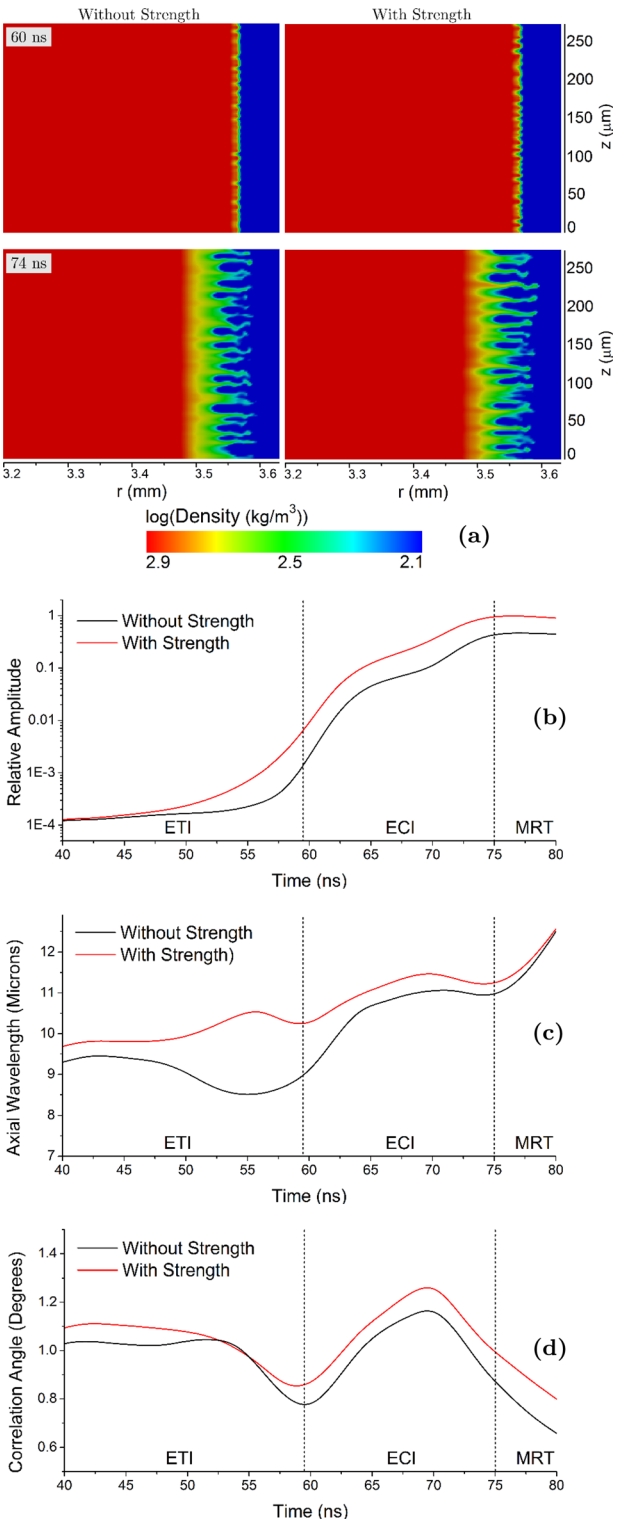

FIG. 13. Density slices showing the effect of material strength on the ECI, scaled to show key values of density (a), with graphs showing normalised total amplitude (b), dominant wavelength (c), and angle of azimuthal correlation (d) calculated via Fourier analysis of unwrapped areal density maps. Strength results in a larger total amplitude, a longer dominant wavelength, and a larger angle of azimuthal correlation.

the simulations of total amplitude, dominant wavelength, and angle of azimuthal correlation shown in Figures 13(b)–13(d), respectively. These were calculated by Fourier analysing the 3D density maps "unwrapped" in the azimuthal direction and integrated in the radial direction. The dominant

wavelength and angle of azimuthal correlation are defined by the mid-points of the spectral energy in the axial and azimuthal directions, respectively; the total amplitude is defined as the integral over all wavelengths of the spectral energy in the axial direction.

The ECI initially becomes visible at 60 ns for both simulations—the peaks are more sharply defined for the simulation with strength and are visible up to a higher density. The difference becomes more pronounced by 74 ns, with a higher spike-bubble amplitude, especially in the more dense material at a radial position of ∼3.5 mm. The amplitudes calculated via Fourier analysis (Figure 13(b)) begin to diverge during the ETI phase. When strength has been lost in the ECI and early MRT phases however, the time dependence is similar for both simulations—the difference can therefore be understood as a constant shift to higher amplitude for the simulation with strength. Similar trends also apply to the axial wavelength (Figure 13(c)) and angle of azimuthal correlation (Figure 13(d)), demonstrating that strength no longer has a direct impact during the ECI and MRT phases, rather the differences between the results are due to the different conditions at the start of the ECI phase, which result from the effect of strength during the ETI phase. This is expected, given that, as shown in Figure 11, strength is lost around the liner outer edge ∼20 ns before the start of the ECI phase. In order to further confirm this hypothesis, another simulation was carried out with material strength switched on for the first 50 ns, after which it was switched off—this gave near identical results to the simulation with strength in Figure 13.

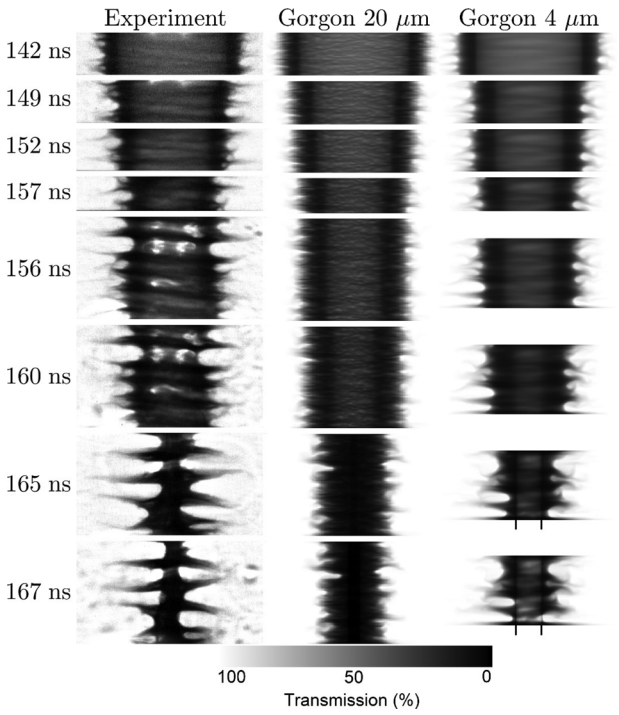

FIG. 14. Comparison of experimental radiographs (column 1)—(Adapted with permission from McBride *et al.*, Phys. Rev. Lett. **109**, 135004 (2012). Copyright 2012 The American Physical Society) to synthetic radiographs from 20 μm Gorgon simulation without material strength (column 2), and 4 μm Gorgon simulation with strength (column 3). Fiducials shown on the final two radiographs for the 4 μm Gorgon results mark the position of the simulation inner boundary.

C. Comparison to experiment

A full circumference, 2 mm long 3D Gorgon simulation with material strength was carried out in cylindrical geometry at a variable resolution. A grid refinement method suggested by Jennings[30] was implemented—a high resolution grid was overlaid on the existing computational grid, with connections between the grids made at two specified radial positions via inter-processor communication. The high resolution grid had double the number of processors and hence resolution in all three directions—this allowed the bulk of the simulation to be run with a resolution of 8 μm in the radial and axial directions, increasing to 4 μm around the liner outer edge to ensure resolution of the ETI, with an azimuthal resolution of 0.3°. Figure 14 shows comparison between resultant synthetic radiographs (column 3), experimental radiographs from Ref. 7 (column 1), and previous randomly initialised Gorgon simulations in Cartesian geometry at 20 μm resolution (insufficient to resolve the ETI, similar to those presented in Ref. 7), as mentioned in Sec. I (column 2).

There is qualitative agreement between experiment and the 4 μm simulation; the MRT wavelengths and amplitudes are comparable, and horizontal banding indicating high levels of azimuthal correlation is visible over the entire time period over which the radiographs were recorded—this is largely absent for the 20 μm Gorgon results. The final two 4 μm radiographs show a vertical cylindrical structure near the centre (marked by fiducials); this is the inner domain boundary of the simulation; at this point the mass of the liner is being lost, affecting inner regions of the liner. However, the features of interest occur around the liner outer edge, a region unlikely to be affected by the lost mass until it stagnates and reflects; we therefore use these results provided the bubble radius is larger than the inner domain boundary. The 20 μm simulation is in Cartesian geometry, so simulates the implosion all the way to the axis.

A quantitative MRT analysis was carried out as in Ref. 7 by Abel inverting the radiographs, allowing the determination of the average liner position and MRT wavelength and amplitude. The normalised liner position is defined by $[1 - r(t)/r_0]$, where $r(t)$ and r_0 are the average MRT bubble position as a function of time and initial position of the liner outer edge, respectively. The MRT properties are plotted in Figure 15 for the experimental results and those from the two simulations.

Figure 15(a) shows that the 20 μm simulation has a consistently lower normalised liner position than the experiment—as there is a much lower level of azimuthal correlation, the MRT develops more slowly and the bubbles enclose more mass so implode more slowly. The inclusion of the early time instabilities in the 4 μm results brings normalised liner position into agreement with the experiment for all but the last two experimental data points—as these were from a different shot, shot-to-shot variance may be a factor and earlier time slices from this shot, z2173,[7] may not match the earlier experimental radiographs presented.

Figures 15(b) and 15(c) show the MRT wavelength and amplitude plotted as functions of normalised liner position; this is preferable to plotting as functions of time as it prevents

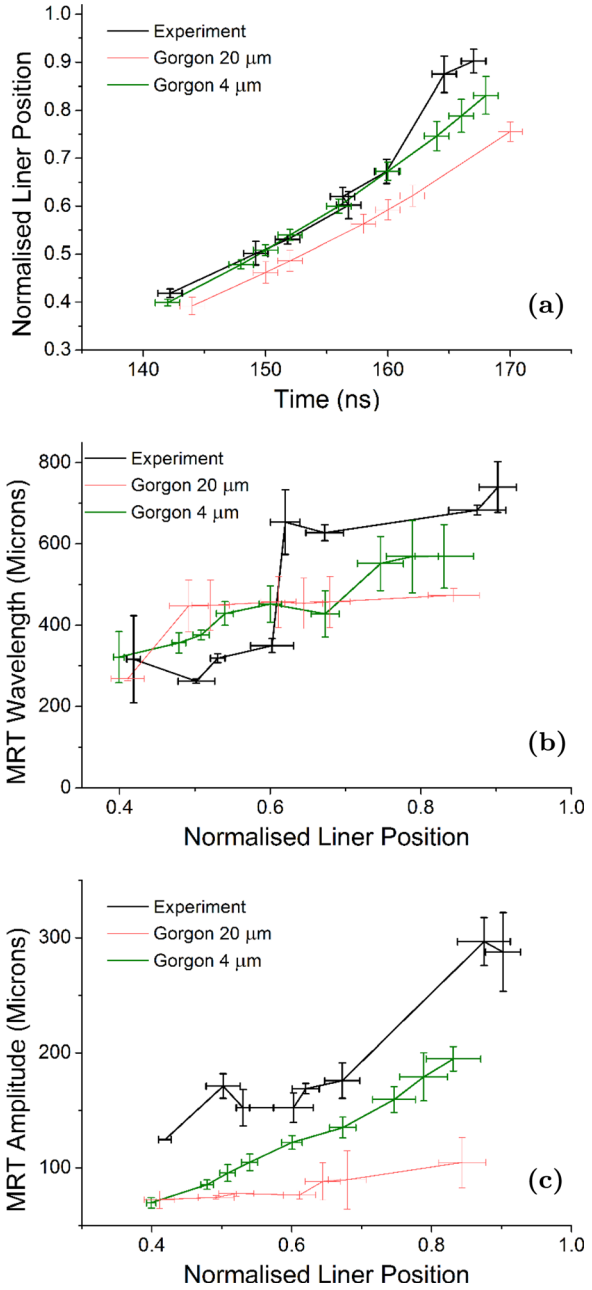

FIG. 15. Normalised liner position and MRT wavelength and amplitude; calculated via Abel analysis of the experiment, 20 μm simulation and 4 μm simulation. Error bars in normalised liner position and MRT amplitude are set to the absolute deviation of the calculated MRT bubble positions; error bars in MRT wavelength derive from the variation between calculated wavelengths using the left and right edges of the radiographs.

uncertainties in timings from affecting the results. For the first four radiographs, the experimental results have a shorter wavelength and higher amplitude than any simulated results; the improvement evident in the 4 μm results over the 20 μm results suggests that this may be because of short wavelength, high amplitude modes near the beginning of the MRT growth phase which are poorly resolved at 20 μm and are better resolved at 4 μm.

At later times, the MRT wavelength and amplitude from the 4 μm simulation are in much better agreement with the experiment than the 20 μm results, but remain lower than those recorded in the experiment. The improvement is primarily due to the increased levels of azimuthal correlation resulting from the early time instabilities, with the flattening off in MRT development evident in the 20 μm results no longer occurring.

The improved treatment of early time instabilities and the liner solid phase has enhanced agreement with experimental results, but there are still discrepancies. The ECI is very sensitive to the equation of state and transport coefficients around vapourisation; as this is a complicated material regime to model, the steep gradients in material properties around this point with respect to density may be inadequately resolved or inaccurate. The equation of state and transport coefficients are also critical during the implosion due to the fast growth rate of the MRT instability.

VI. CONCLUSIONS

Over the course of this work, we have developed an improved understanding of the seeding and development of the MRT instability that is critical to the success of MagLIF as a fusion scheme. We have demonstrated the process by which the ETI develops azimuthal correlation, from both single point and random perturbations. We provide a physical explanation for the development of the ECI at vapourisation, with subsequent development of the ECI and MRT instability having been demonstrated in a 3D simulation, which also shows how material of different densities dominates instability development at different times.

We have demonstrated the importance of material strength during the development of the early time instabilities for MagLIF-relevant liner implosions which later seed the MRT instability. Strength is important both for its role in setting an increased ETI wavelength and amplitude during the solid phase, and for maintaining the liner outer edge at a higher density prior to vapourisation; the combination of which results in an increased ECI amplitude and wavelength.

The sum of these effects applied to high resolution, full circumference simulations, have partially explained the large MRT amplitudes and wavelengths observed by McBride *et al.*,[7] primarily due to the development of early time azimuthal correlation which is subsequently imprinted on the material comprising the liner outer edge during vapourisation. These simulations have achieved better agreement with the experimental results than previous 3D simulations which did not resolve the ETI or include material strength, with excellent agreement reached for normalised liner position, good agreement for MRT wavelength, and reasonable agreement for the rate of increase of the MRT amplitude, although absolute values were still under-estimated.

We plan to further investigate the development of early time azimuthal correlation; in particular, the ability of low density plasma formed by the desorption of contaminants early in time to imprint structures onto the liner outer edge prior to vapourisation.

ACKNOWLEDGMENTS

The authors wish to thanks Gareth Collins from Imperial College London and Christopher Jennings, Ryan McBride, and Kyle Peterson from Sandia National Laboratories for

useful discussions. Full circumference simulations were carried out on the UK national supercomputer, ARCHER. This work was supported by EPSRC and AWE Aldermaston.

[1]S. A. Slutz, M. C. Herrmann, R. A. Vesey, A. B. Sefkow, D. B. Sinars, D. C. Rovang, K. J. Peterson, and M. E. Cuneo, "Pulsed-power-driven cylindrical liner implosions of laser preheated fuel magnetized with an axial field," Phys. Plasmas **17**(5), 056303 (2010).
[2]S. A. Slutz and R. A. Vesey, "High-gain magnetized inertial fusion," Phys. Rev. Lett. **108**, 025003 (2012).
[3]S. Chandrasekhar, *Hydrodynamic and Hydromagnetic Stability* (Oxford University Press, London, 1961), p. 429.
[4]E. G. Harris, "Rayleigh-Taylor instabilities of a collapsing cylindrical shell in a magnetic field," Phys. Fluids **5**(9), 1057–1062 (1962).
[5]M. K. Matzen, B. W. Atherton, M. E. Cuneo, G. L. Donovan, C. A. Hall, M. Herrmann, M. L. Kiefer, R. J. Leeper, G. T. Leifeste, F. W. Long, G. R. Mckee, T. A. Mehlhorn, J. L. Porter, L. X. Schneider, K. W. Struve, W. A. Stygar, and E. A. Weinbrecht, "The refurbished z facility: Capabilities and recent experiments," Acta Phys. Pol., A **115**, 956–958 (2009).
[6]M. E. Cuneo, M. C. Herrmann, D. B. Sinars, S. A. Slutz, W. A. Stygar, R. A. Vesey, A. B. Sefkow, G. A. Rochau, G. A. Chandler, J. E. Bailey, J. L. Porter, R. D. McBride, D. C. Rovang, M. G. Mazarakis, E. P. Yu, D. C. Lamppa, K. J. Peterson, C. Nakhleh, S. B. Hansen, A. J. Lopez, M. E. Savage, C. A. Jennings, M. R. Martin, R. W. Lemke, B. W. Atherton, I. C. Smith, P. K. Rambo, M. Jones, M. R. Lopez, P. J. Christenson, M. A. Sweeney, B. Jones, L. A. McPherson, E. Harding, M. R. Gomez, P. F. Knapp, T. J. Awe, R. J. Leeper, C. L. Ruiz, G. W. Cooper, K. D. Hahn, J. McKenney, A. C. Owen, G. R. McKee, G. T. Leifeste, D. J. Ampleford, E. M. Waisman, A. Harvey-Thompson, R. J. Kaye, M. H. Hess, S. E. Rosenthal, and M. K. Matzen, "Magnetically driven implosions for inertial confinement fusion at Sandia National Laboratories," IEEE Trans. Plasma Sci. **40**(12), 3222–3245 (2012).
[7]R. D. McBride, S. A. Slutz, C. A. Jennings, D. B. Sinars, M. E. Cuneo, M. C. Herrmann, R. W. Lemke, M. R. Martin, R. A. Vesey, K. J. Peterson, A. B. Sefkow, C. Nakhleh, B. E. Blue, K. Killebrew, D. Schroen, T. J. Rogers, A. Laspe, M. R. Lopez, I. C. Smith, B. W. Atherton, M. Savage, W. A. Stygar, and J. L. Porter, "Penetrating radiography of imploding and stagnating beryllium liners on the *z* accelerator," Phys. Rev. Lett. **109**, 135004 (2012).
[8]R. D. McBride, M. R. Martin, R. W. Lemke, J. B. Greenly, C. A. Jennings, D. C. Rovang, D. B. Sinars, M. E. Cuneo, M. C. Herrmann, S. A. Slutz, C. W. Nakhleh, D. D. Ryutov, J.-P. Davis, D. G. Flicker, B. E. Blue, K. Tomlinson, D. Schroen, R. M. Stamm, G. E. Smith, J. K. Moore, T. J. Rogers, G. K. Robertson, R. J. Kamm, I. C. Smith, M. Savage, W. A. Stygar, G. A. Rochau, M. Jones, M. R. Lopez, J. L. Porter, and M. K. Matzen, "Beryllium liner implosion experiments on the z accelerator in preparation for magnetized liner inertial fusion," Phys. Plasmas (1994-present) **20**(5), 056309 (2013).
[9]J. P. Chittenden, S. V. Lebedev, C. A. Jennings, S. N. Bland, and A. Ciardi, "X-ray generation mechanisms in three-dimensional simulations of wire array z-pinches," Plasma Phys. Controlled Fusion **46**(12B), B457 (2004).
[10]A. Ciardi, S. V. Lebedev, A. Frank, E. G. Blackman, J. P. Chittenden, C. J. Jennings, D. J. Ampleford, S. N. Bland, S. C. Bott, J. Rapley, G. N. Hall, F. A. Suzuki-Vidal, A. Marocchino, T. Lery, and C. Stehle, "The evolution of magnetic tower jets in the laboratory," Phys. Plasmas **14**(5), 056501 (2007).
[11]D. B. Sinars, S. A. Slutz, M. C. Herrmann, R. D. McBride, M. E. Cuneo, K. J. Peterson, R. A. Vesey, C. Nakhleh, B. E. Blue, K. Killebrew, D. Schroen, K. Tomlinson, A. D. Edens, M. R. Lopez, I. C. Smith, J. Shores, V. Bigman, G. R. Bennett, B. W. Atherton, M. Savage, W. A. Stygar, G. T. Leifeste, and J. L. Porter, "Measurements of magneto-Rayleigh-Taylor instability growth during the implosion of initially solid Al tubes driven by the 20-MA, 100-ns Z facility," Phys. Rev. Lett. **105**, 185001 (2010).
[12]D. D. Ryutov, M. S. Derzon, and M. K. Matzen, "The physics of fast Z pinches," Rev. Mod. Phys. **72**, 167–223 (2000).
[13]K. J. Peterson, D. B. Sinars, E. P. Yu, M. C. Herrmann, M. E. Cuneo, S. A. Slutz, I. C. Smith, B. W. Atherton, M. D. Knudson, and C. Nakhleh, "Electrothermal instability growth in magnetically driven pulsed power liners," Phys. Plasmas **19**(9), 092701 (2012).
[14]K. J. Peterson, E. P. Yu, D. B. Sinars, M. E. Cuneo, S. A. Slutz, J. M. Koning, M. M. Marinak, C. Nakhleh, and M. C. Herrmann, "Simulations of electrothermal instability growth in solid aluminum rods," Phys. Plasmas (1994-present) **20**(5), 056305 (2013).
[15]V. I. Oreshkin, "Thermal instability during an electrical wire explosion," Phys. Plasmas **15**(9), 092103 (2008).
[16]V. I. Oreshkin, "Overheat instabilities in the electric explosion of wires," Tech. Phys. Lett. **35**(1), 36–39 (2009).
[17]S. Faik, M. M. Basko, A. Tauschwitz, I. Iosilevskiy, and J. A. Maruhn, "Dynamics of volumetrically heated matter passing through the liquid vapor metastable states," High Energy Density Phys. **8**(4), 349–359 (2012).
[18]A. J. Kemp and J. Meyer ter Vehn, "An equation of state code for hot dense matter, based on the {QEOS} description," Nucl. Instrum. Methods Phys. Res., Sect. A **415**(3), 674–676 (1998).
[19]R. M. More, K. H. Warren, D. A. Young, and G. B. Zimmerman, "A new quotidian equation of state (QEOS) for hot dense matter," Phys. Fluids (1958–1988) **31**(10), 3059–3078 (1988).
[20]Y. T. Lee and R. M. More, "An electron conductivity model for dense plasmas," Phys. Fluids (1958–1988) **27**(5), 1273–1286 (1984).
[21]M. P. Desjarlais, "Practical improvements to the Lee-More conductivity near the metal-insulator transition," Contrib. Plasma Phys. **41**(2–3), 267–270 (2001).
[22]A. Amsden, H. Ruppel, and C. Hirt, "SALE: A simplified ale computer program for fluid flow at all speeds," Los Alamos National Laboratories Report No. LA-8095, 101 p, Los Alamos, New Mexico, 1980.
[23]G. S. Collins and H. J. Melosh, "Sales_2: A multi-material hydrocode with elasticplastic strength model and Grady-Kipp fragmentation algorithm."
[24]G. S. Collins, H. Jay Melosh, and B. A. Ivanov, "Modeling damage and deformation in impact simulations," Meteorit. Planet. Sci. **39**(2), 217–231 (2004).
[25]K. Wunnemann, G. S. Collins, and H. J. Melosh, "A strain-based porosity model for use in hydrocode simulations of impacts and implications for transient crater growth in porous targets," Icarus **180**(2), 514–527 (2006).
[26]G. R. Johnson and W. H. Cook, "Fracture characteristics of three metals subjected to various strains, strain rates, temperatures and pressures," Eng. Fract. Mech. **21**(1), 31–48 (1985).
[27]N. G. W. Cook, J. C. Jaeger, and R. W. Zimmerman, *Fundamentals of Rock Mechanics*, 4th ed. (Blackwall Publishing, 2007), Chap. 2.
[28]G. Collins, "Numerical modelling of large impact crater collapse," Ph.D. thesis (Department of Earth Science and Engineering, Imperial College of Science, Technology and Medicine, University of London, 2002).
[29]E. Pierazzo, N. Artemieva, E. Asphaug, E. C. Baldwin, J. Cazamias, R. Coker, G. S. Collins, D. A. Crawford, T. Davison, D. Elbehausen, K. A. Hosapple, K. R. Housen, D. G. Korycansky, and K. Wunnemann, "Validation of numerical codes for impact and explosion cratering: Impacts on strengthless and metal targets," Meteorit. Planet. Sci. **43**(12), 1917–1938 (2008).
[30]C. Jennings, personal communication (2004).